RSC Advances

This is an *Accepted Manuscript*, which has been through the Royal Society of Chemistry peer review process and has been accepted for publication.

Accepted Manuscripts are published online shortly after acceptance, before technical editing, formatting and proof reading. Using this free service, authors can make their results available to the community, in citable form, before we publish the edited article. This *Accepted Manuscript* will be replaced by the edited, formatted and paginated article as soon as this is available.

You can find more information about *Accepted Manuscripts* in the Information for Authors.

Please note that technical editing may introduce minor changes to the text and/or graphics, which may alter content. The journal's standard Terms & Conditions and the Ethical guidelines still apply. In no event shall the Royal Society of Chemistry be held responsible for any errors or omissions in this *Accepted Manuscript* or any consequences arising from the use of any information it contains.

ROYAL SOCIETY OF CHEMISTRY

www.rsc.org/advances

Please do not adjust margins

Journal Name

ARTICLE

Solar and visible light photocatalytic enhancement of halloysite nanotubes / g-C_3N_4 heteroarchitectures

Received 00th January 20xx,
Accepted 00th January 20xx

DOI: 10.1039/x0xx00000x

www.rsc.org/

K. C. Christoforidis,[a,*] M. Melchionna,[a] T. Montini,[a] D. Papoulis,[b] E. Stathatos,[c] S. Zafeiratos,[d] E. Kordouli[e] and P. Fornasiero[a,*]

Novel heteroarchitectures made of graphitic carbon nitride (g-C_3N_4) and halloysite nanotubes (HNTs) were prepared by a facile and soft self-assembly strategy. The morphological, structural and electronic properties of the HNTs/g-C_3N_4 nanocomposites were determined by means of a plethora of techniques including N_2 physisorption, XRD, FT-IR, TEM, UV-Vis absorption, XPS, ζ potential and photoluminescence (PL). Their photocatalytic activity was evaluated under both simulated solar light and pure visible light irradiation against the photodegradation of neutral positively and negatively charged pollutants, namely phenol, methylene blue (MB) and methyl orange (MO), respectively. The prepared HNTs/g-C_3N_4 nanocomposites were proven to be durable and significant more efficient than the pure g-C_3N_4 reference for the degradation of positively charged and neutral organics. The nanocomposites presented increased charge carrier formation and reduced recombination rate due to the tight contact between the two components. The enhanced photoactivity was attributed to the dual function of HNTs enhancing a) the abundance and stability of the photogenerated e^- and h^+ pairs and b) the adsorption of positively charged organics on the nanocomposite. Both functions originate from the charged surface of HNTs.

Introduction

Photocatalysis using semiconductor materials has received a lot of attention during the past decades as a suitable method for environmental protection,[1] green synthesis[2,3] and sustainable energy production.[4] Numerous materials have been prepared and applied, mostly based on metal oxides.[5-7] However, despite the great effort, the development of stable, environmental-friendly and efficient photocatalysts under solar light irradiation is still a significant challenge for realistic applications. Recently, the metal-free polymeric semiconductor graphite-like carbon nitride (g-C_3N_4) has attracted great attention due to its successful application in a variety of photo-initiated reactions under either UV, UV-visible or pure visible-light irradiation.[8-10] g-C_3N_4 is a low cost, non-toxic and simple to synthesize material, presenting excellent chemical and thermal stability and relatively narrow band gap energy (~2.7 eV).[11,12]

Different strategies have been developed for the synthesis of pure and modified (e.g. functionalized) g-C_3N_4 including shape modification.[13,14] Pure g-C_3N_4 suffers from fast recombination rates of the photogenerated charge carries (electron/hole pairs, e^-/h^+) and small specific surface area.[12] Recent attempts have been made to eliminate these inherent drawbacks including doping,[15,16] functionalization with metal nanoparticles,[18] control of morphology and thickness[18-21] as well as development of composites and heterostructures.[22-28] Nevertheless, the reported photocatalytic activities vary significantly depending on the synthesis process applied.

In the field of photocatalysis, the synthesis of heterostructures and composites via the coupling of photocatalysts with even non-photoactive materials has been shown to improve significantly photoactivity as well as surface area. To this scope, a large variety of materials have been coupled with photocatalysts including among others silica, carbon nanotubes, graphene, organic polymers and clay minerals.[26-35] Among them, the utilization of clay minerals is a particularly interesting approach since they are low cost and readily available natural materials, non-toxic, easily accessible and environmental friendly, suitable for the development of green materials.[26,32-36] Nanocomposites made of photocatalysts and clay minerals, have been recently studied for air decontamination and organic pollutants degradation.[32-35] Surprisingly, layered clay minerals have been more investigated than one-dimensional clay minerals (i.e. fibrous or tubular) despite they require an exfoliation step.

[a] Department of Chemical and Pharmaceutical Sciences, ICCOM-CNR Trieste Research Unit and INSTM Research Unit, University of Trieste, via L. Giorgieri 1, 34127 Trieste, Italy. E-mail: pfornasiero@units.it, kchristoforidis@units.it; Tel: +39 0405583973.
[b] Department of Geology, University of Patras, 26504 Patras, Greece.
[c] Department of Electrical Engineering, Technological Educational Institute (TEI) of Western Greece, 26334 Patras, Greece.
[d] Institut de Chimie et Procédés Pour l'Energie, l'Environnement et la Santé, (ICPEES) ECPM, University of Strasbourg, 25 rue Becquerel Cedex 2, 67087 Strasbourg, France.
[e] Department of Chemistry, University of Patras, 26504 Patras, Greece.
Electronic Supplementary Information (ESI) available: XPS spectra, N_2 isotherms, pore size distribution, TGA analysis, UV-Vis absorption spectra, ζ potential analysis, MB adsorption, photocatalytic kinetic-plots, photocatalytic degradation of phenol and MO. See DOI: 10.1039/x0xx00000x

RSC Advances Accepted Manuscript

Please do not adjust margins

Halloysite is a naturally occurring aluminosilicate clay material clay with a unit formula $Al_2Si_2O_5(OH)_4 \cdot 2H_2O$ presenting tubular morphology.[37] Halloysite nanotubes (HNTs) are abundant, can be obtained as a raw mineral and therefore are available at low cost, are non-toxic even at high concentrations, have relatively high specific surface area and charged surface.[38] The internal surface is composed of a gibbsite-like array of Al–OH groups and the external of Si–O–Si groups, containing adequate surface –OH groups.[39] The charge distribution (positive inner and negative outer surface) and the nano-sized structure of tubular morphology has triggered sophisticated applications of such materials in drug delivery,[40] catalysis,[33] adsorption,[41] encapsulation and storage of molecules (nano-containers)[38,42] and as template.[43] In the case of catalysis, HNTs have been proven suitable support for the development of composites with superior activity for energy related reactions,[44] antimicrobial activity,[43] and organics degradation.[32,35] The enhanced activity is attributed to various factors such as high dispersion of the supported/immobilized catalyst increasing its active surface, increased dispersion of the composite in suspensions, improved light absorption properties and synergistic effects. Recently, ternary nanocomposite materials prepared through the coupling of halloysite nanotubes with ZnO and g-C_3N_4 were developed using a two-pot synthesis process and applied for the photocatalytic degradation of tetracycline.[28] The enhanced activity was primarily linked with the efficient charge separation due to the matched band edge potentials of g-C_3N_4 and ZnO.

It is clear, therefore, that the utilization of natural clay minerals as support or even coupled with semiconducting catalysts presents clear advantages over synthesized materials. Very recently, bentonite/g-C_3N_4 composites were synthesized and applied for the photodegradation of MB dye presenting 2.5 higher photoactivity compared to the g-C_3N_4 reference material.[31] Herein, in search of environmental friendly, biocompatible and solar-light active photocatalysts with improved properties, we have investigated the potential to couple natural HNTs with g-C_3N_4 towards the development of nanocomposites. A series of HNTs/g-C_3N_4 samples were prepared by varying the HNTs content and applied for the degradation of neutral, positively and negatively charged organic substrates under both simulated solar light and pure visible light irradiation. The nanocomposites presented superior photoactivity compared to the g-C_3N_4 reference. The work focused also on mechanistic aspects of reactivity related with the photogenerated charges and the reactive species participating in photocatalysis. The enhanced photoactivity is primarily linked with the efficient charge migration and separation in the heteroarchitectures while the increased adsorption of positively charged molecules further increases reactivity. Both functions are driven by the HNTs charged surface.

Experimental

Materials and reagents

Melamine, methylene blue (MB – 3,7-bis(dimethylamino) phenazathionium chloride), methyl orange (MO – 4-[4-(dimethylamino) phenylazo] benzenesulfonic acid sodium salt), phenol and isopropanol (IPA) (99.8) were purchased from Sigma-Aldrich. *tert*-butyl alcohol (TBA) (99%) was purchased from Fluka. All chemicals were used without any further purification. A HNTs sample obtained from Utah, USA was used.[32] The sample was size fractionated to obtain particles < 2 μm by gravity sedimentation and the clay fraction was carried out by centrifugation. The clay fraction of the sample was used for the preparation of the nanocomposites in order to avoid the presence other mineral impurities.

Synthesis process

Graphitic carbon nitride was synthesized via thermal polycondensation of melamine.[10] Melamine was put into an alumina crucible with a cover and heated in air at 540 ^oC in a muffle furnace for 4 h with a heating rate of 5 ^oC min^{-1}. The material was collected and milled into powder in a mortar.

The HNTs/g-C_3N_4 nanocomposites were synthesized *via* a simple and soft self-assembly strategy. First, the parent g-C_3N_4 (0.6 g in 100 ml of double-distilled water) was exfoliated through sonication for 2 h at room temperature. An aqueous suspension containing a proper amount of HNTs sonicated for 1 h was added to the above suspension, further sonicated for 1 h and then stirred overnight. The light yellowish powder was collected by filtration and washed with acetone. Finally the material was dried over night at 90 ^oC. Hereafter, the nanocomposites are labeled CNH-*x*, where the increasing *x* value indicates the increasing nominal fraction of HNTs in the final material. Materials containing 2, 4, 6 and 10 nominal wt.% of HNTs were prepared. CN stands for the pure g-C_3N_4 sample prepared *via* the same process but in the absence of HNTs. The reproducibility of the synthesis process applied was tested by preparing the nanocomposite containing the highest HNTs amount (i.e. CNH-4) two times. The FT-IR spectra and TGA profiles (HNTs content 9.3 and 9.5%) of the two materials were identical (data not shown).

Materials characterization

Thermogravimetric analysis (TGA) was performed with a TGA Q500 (TA Instruments) under air flow, from 100 to 800 ^oC with a heating rate of 10 ^oC min^{-1}. The composition of the nanocomposites was calculated from the weight difference between 200 and 700 ^oC. Nitrogen adsorption-desorption isotherms were obtained at the liquid nitrogen temperature using a Micrometrics ASAP 2020 system. Each sample was degassed at 170^oC overnight before measurements. The Brunauer-Emmett-Teller (BET) model was used to determine the specific surface area. Fourier transform infrared (FT-IR) spectra in the 4000-400 cm^{-1} region were recorded using KBr pellets with a Perkin Elmer 2000 instrument. TEM measurements were performed on a TEM Philips EM208, using an acceleration voltage of 100 kV. Samples were prepared by drop casting the dispersed particles onto a TEM grid (200 mesh, copper, carbon only). X-ray diffraction patterns were collected with a Philips X'Pert diffractometer with a Cu Ka X-

RSC Advances Accepted Manuscript

 This journal is © The Royal Society of Chemistry 20xx

ray source. Photoluminescence spectra of the prepared catalysts were recorded with a Hitachi F-2500 fluorophotometer. The samples were excited at 360 nm. A Zetasizer 5000 (Malvern Instruments Ltd) microelectrophoresis apparatus was used to determine the ζ potential in an electrolytic suspension. The values of the ζ potential were determined in a pH range of 2.2-6.2 using 100 mL of suspension, containing 0.01 g of solid, with an ionic strength of 0.01 mol L^{-1} KNO_3 at 25°C. Details for the experimental procedure can be found elsewhere.[45] The X-ray photoelectron spectroscopy (XPS) measurements were carried out in an ultrahigh vacuum (UHV) spectrometer equipped with a VSW Class WA hemispherical electron analyzer. A monochromatic Al Kα X-ray source (1486.6 eV) was used as incident radiation. Survey and high resolution spectra were recorded in constant pass energy mode (90 and 44 eV, respectively). UV-visible diffuse reflectance spectra were recorded with a PerkinElmer (Lamda 35) spectrophotometer equipped with an integrating sphere assembly with a nominal resolution of 1 nm using $BaSO_4$ as reference. The band gap energies were estimated from samples' optical absorption edges using the following formula:

$$ahv=B(hv-E_g)^2$$

where hv, α and B represent the excitation energy, absorption coefficient and a constant, respectively. Instead of a, the Kubelka-Munk function was applied in order to eliminate any tailing contribution from the DR-UV-Vis spectra.[46] The following function was applied to convert the absorption spectra:

$$F(R)=\frac{(1-R)^2}{2R}$$

where R is the reflectance. The E_g values were estimated from the plot of $F(R)hv^2$ versus energy by extrapolating the linear part.

Photocatalytic degradation

The photocatalytic activity of the prepared catalysts was evaluated against the degradation of cationic and anionic dyes (MB and MO respectively) and phenol in aqueous solution. Catalytic tests were performed under both simulated solar light (300 W Xe Arc light source system with standard 1.5 AM filter) and pure visible light irradiation using a 420 nm cut-off filter. The catalyst (1.25 g L^{-1} for dyes and 2 g L^{-1} for phenol) and 160 ml of aqueous 10 mg L^{-1} dye or 5 mg L^{-1} phenol solution were placed in a Teflon reactor and the reaction temperature was maintained at 20 °C by using a VWR Cryostat (1160S). Prior to irradiation, the suspension was stirred for 1.5 h in the dark to reach the adsorption equilibrium. For the quantification of the dyes, aliquots (2 ml) of the suspension were periodically taken and filtered through a 0.45 μm PTFE Millipore disc. To quantify phenol, 3 ml aliquots were drawn and centrifuged at 4500 rpm at certain time intervals. UV/Vis spectroscopy was used to determine the dye's concentration. Concentration of phenol was determined by HPLC at 270 nm. Quantification was based on comparison with standards. For the recycling experiments, the used catalyst was collected,

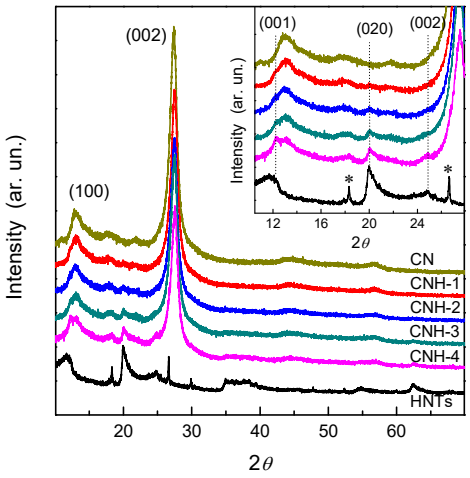

Fig. 1 XRD patterns of g-C_3N_4, HNTs and CNH-x nanocomposites. Inset: close view indicating the most intense reflections of HNTs. The symbols at 18.4° and 26.6° 2ϑ indicate alunite and quartz impurities in the HNTs, respectively.

washed with water three consecutive times under stirring, washed with acetone and finally dried over night at 90 °C. At this point we highlight that catalytic activity is greatly affected by the actual setup used. Mechanistic aspects of the catalytic reaction were studied by using IPA and TBA (0.2 mmol) as h^+ and hydroxyl radical ($OH^{\cdot}$) scavengers, respectively. Argon was used to study the effect of superoxide radical ($O_2^{-\cdot}$) formation on photoactivity.

Results and discussion

Characterization of photocatalysts

Fig. 1 shows XRD patterns of g-C_3N_4, HNTs and the HNTs/g-C_3N_4 nanocomposites. All g-C_3N_4 containing samples exhibit the two characteristic reflections at approximately 12.9° and 27.4° 2ϑ corresponding to the (100) and (002) crystal planes of g-C_3N_4. These two features confirmed the formation of the graphitic stacking structure. In addition, a gradual decrease of the main diffraction peak intensity with increasing HNTs content is observed, suggesting interaction between the two components of the nanocomposite. In the case of HNTs, the diffraction pattern contains all the characteristic reflections of halloysite.[43] As reported in the inset in Fig. 1, the main reflections of HNTs are observed in all CNH-x samples, suggesting that the HNTs structure is maintained unaltered in the nanocomposites.

FT-IR spectra of the g-C_3N_4, CNH-x and HNTs are shown in Fig. 2. All characteristic peaks of g-C_3N_4 are detected in the g-C_3N_4 and HNTs/g-C_3N_4 spectra. The stretching vibration of N–H bonds (primary (–NH_2) and secondary (=N–H) amines) are observed at high wavenumber (~3200 cm^{-1}). The typical stretching vibration modes of heptazine heterocyclic ring are detected in the 1200-1680 cm^{-1} region while the sharp absorption peak at 806 cm^{-1} is characteristic of the breathing mode of the triazine units. For the pure HNTs the bands at

RSC Advances Accepted Manuscript

3696 and 3623 cm^{-1} are assigned to the O–H vibrations of the Al–OH at the inner surface. The bands at 1117 cm^{-1}, 1086 cm^{-1} and 1033 cm^{-1} correspond to the Si–O stretching vibration bands.[44,47] The band at 912 cm^{-1} corresponds to the O–H deformation vibration of the inner Al–OH groups. The stretching vibration at 3480 cm^{-1} is ascribed to interlayer or adsorbed water on HNTs with the corresponding deformation vibration at 1640 cm^{-1}.[44] The bands of the pure g-C_3N_4 and the main bands of the HNTs are present in the CNH-*x* nanocomposites, verifying that the structural features of the parent materials remain intact during the preparation of the nanocomposites, in agreement with XRD data. From the observed HNTs bands in the CNH-x composites, the bands corresponding to the inner surface of the HNTs (i.e. those related with the Al–OH) are unaltered while a clear shift of the Si–O broad stretching band from 1033 cm^{-1} to 1040 cm^{-1} is observed (see inset in Fig. 2), in accordance with a tight interaction between the g-C_3N_4 and the outer surface of HNTs.[32,35,44]

XPS data provides further information on the composition of the prepared materials. The survey scan XPS spectra of the pure g-C_3N_4, HNTs and the CNH-2 nanocomposite are given in Fig. S1. In the case of the HNTs sample, the peaks corresponding to Si, Al and O are detected together with a small amount of C. The CN sample is characterized by the two dominant peaks of C and N while in the nanocomposites additional Al and Si peaks were also detected due to HNTs, in agreement with the XRD and FT-IR data. High resolution XPS spectra of C1s, N 1s, O 1s, Al 2p and Si 2p spectra were also acquired (Fig. 3 and S2). The N 1s peak of both pure CN reference and the nanocomposites samples appears at 398.8 eV and is characteristic of sp^2 hybridised nitrogen.[22,48] In the C 1s spectra two peaks can be distinguished. The dominant C 1s peak centered at ca. 288.4 eV is due to sp^2-bonded carbon (C=N), while the components at lower BEs are due to hydroxylized/oxidized groups and adventitious carbon species.[49] The composites have identical O 1s peaks, however as compared to the O 1s measured on pure HNTs, they both have an additional shoulder at lower BEs, due to the presence of CN. The low BE component at ca. 532.2 eV (Fig. S2C), is located at about 0.8 eV lower BE relative to the O 1s peak of the pure CN material, suggesting a chemical interaction between HNTs and g-C_3N_4. The Al 2p peak of the nanocomposites is centered at ca. 75.9 eV without evident differences with that of the pure HNTs (Fig. S2D).

The Si 2p XPS spectra of the HNTs and the CNH-*x* nanocomposites is composed by two peaks (Fig. 3). For the pure HNTs the two peaks were centered at ca. 104.3 and 101.5 eV and have been previously assigned to SiO_2 and Si-OH species, respectively.[50] In the nanocomposites, the SiO_2 peak remains fixed at 104.3 eV, while the second peak appears shifted to higher BEs (ca. 101.9 and 102.1 eV for the CNH-4 and CNH-2 respectively). The BE shift of the chemical species located at the outer side of HNTs lumens indicates a possible interaction with g-C_3N_4. This observation is in line with the changes observed on the O 1s peaks of the composite materials and may be related with the interaction of the silanol

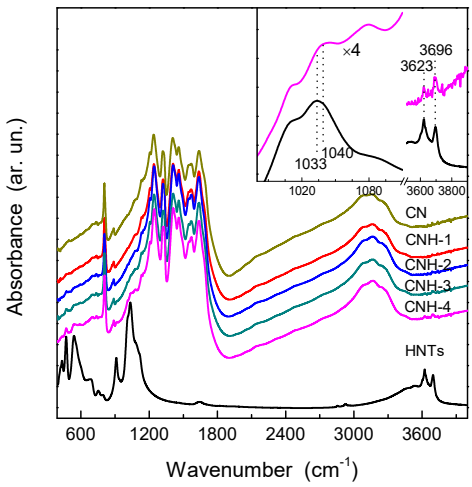

Fig. 2 FT-IR spectra of g-C_3N_4, HNTs and CNH-*x* nanocomposites. Inset: close view.

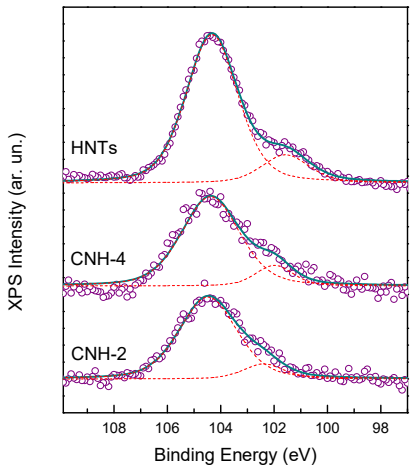

Fig. 3 High resolution Si 2p XPS spectra of the pure HNTs and the CNH-2 and CNH-4 nanocomposites. Symbols: experimental data; lines: fittings.

groups on the external surface of HNTs with N-containing groups of g-C_3N_4. BE shifts of the S–OH peak have been previously observed during HNTs surface modification.[51]

The nitrogen adsorption and desorption isotherms and the BJH pore-size distribution curves are presented in Fig. S3 and S4, respectively. The pure materials show the typical isotherms of halloysite and g-C_3N_4. HNTs present a mesoporous structure, with a bimodal pore size distribution centered approximately at 3-4 nm and 8.5-10.5 nm. A bimodal pore size distribution is also observed for the samples containing g-C_3N_4 (i.e. CN and CNH-*x* samples), with a main contribution in the range 3.5-4 nm and a second and broader centered at about 10-20 nm. The average pore size of the second contribution in the nanocomposites presents a clear tendency towards lower values with increasing HNTs content, reaching the value observed for the pure HNTs (Fig. S4). Table 1 summarizes the BET surface area, total pore volume and the average pore size

RSC Advances Accepted Manuscript

This journal is © The Royal Society of Chemistry 20xx

Table 1 Characteristics of the prepared nanomaterials.

Sample	BET (m^2/g)	Pore volume (cm^3/g)	Average Pore size (nm)	HNTs wt.% [a]	E_g (eV)
CN	5	0.044	15.0		2.76
CNH-1	8	0.054	13.8	1.4 (2)	2.79
CNH-2	9	0.064	12.7	3.4 (4)	2.80
CNH-3	9	0.058	12.5	5.5 (6)	2.79
CNH-4	12	0.072	11.0	9.3 (10)	2.80
HNTs	55	0.160	10.0		

[a] Calculated from the TGA profiles. The values in parenthesis correspond to the nominal HNTs content.

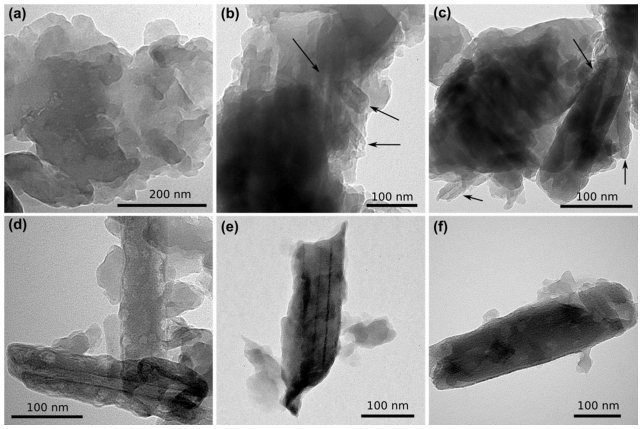

Fig. 4 Representative TEM images of the g-C_3N_4 (a) and the CNH-*x* heteroarchitectures (CNH-1 (b), CNH-2 (c), CNH-3 (d), CNH-4 (e) and (f)). Arrows point the HNTs.

of the nanocomposites and pure materials. An increase of both BET surface area and pore volume is observed in the CNH-*x* nanocomposites with respect to the case of pure g-C_3N_4, confirming that the introduction of HNTs favors specific surface area increase.

Transmission electron microscopy was used to study the morphology of the as-prepared g-C_3N_4 and CNH-*x* nanocomposites. Representative images are given in Fig. 4. g-C_3N_4 shows the typical layered structure with relatively large sized sheets. HNTs present the typical tubular structure with about 70 nm average diameter and a lumen of about 14 nm. In the TEM images of the nanocomposites it is possible to easily recognize the tubular and layered structure of HNTs and g-C_3N_4, respectively. HNTs were detected on the g-C_3N_4 sheets but also covered with relatively large g-C_3N_4 sheets (Fig. 4b and c). Nevertheless, comparing the heteroarchitectures with that of the pure g-C_3N_4, many thin and small g-C_3N_4 sheets were detected on the surface of HNTs, clearly observed in the nanocomposites with high HNTs content (Fig. 4d, e and f). These small sized g-C_3N_4 sheets interact with HNTs covering their external surface, in agreement with FT-IR and XPS. On the contrary, pure HNTs presented smooth surface. Some isolated HNTs were also detected for the CNH-4 sample, e.g. the sample containing high HNTs content. In addition, the HNTs are well dispersed and no agglomerates were detected. This observation clearly suggests that the dispersion of the g-C_3N_4 is increased in the nanocomposites *via* the formation of small sized layers attached on the surface of HNTs. Overall, the TEM study revealed that the soft self-assembly synthesis process adopted herein resulted in the formation of nanocomposites with tight interaction between the two parts while at the same time preserving the morphology of the parent materials.

The thermal stability and the composition of the prepared materials were investigated by means of thermogravimetric analysis (Fig. S5). No significant weight loss was observed for the pure HNTs. The onset of the decomposition temperature for the pure g-C_3N_4 is about 560°C. The corresponding onset for the CNH-*x* nanocomposites is lower (i.e. 540°C) which may originate from the thinner and smaller g-C_3N_4 sheets observed on the surface of HNTs. However, the temperature for the complete decomposition is slightly shifted to higher values with increasing HNTs content in the final nanocomposite. For example, pure g-C_3N_4 is completely decomposed at 670°C while CNH-4 at 700°C. This observation indicates that HNTs act as thermal barriers or stabilize the g-C_3N_4, hindering the thermal degradation, as previously observed in the case of bentonite/g-C_3N_4[26], polymer/HNTs[52] and graphene/g-C_3N_4 composites.[53] The amount of inorganic residue which is directly related to the HNTs content was calculated from the TGA (Table 1).

Light absorption properties were studied by UV-Vis spectroscopy. Fig. S6A displays the UV-Vis absorption spectra of the prepared materials obtained from the DR-spectra. The absorption edge of the pure g-C_3N_4 material is around 450 nm corresponding to band gap energy (E_g) of 2.76 eV, in agreement with values reported in the literature for pure g-C_3N_4.[8] All CNH-*x* nanocomposites exhibited E_g in a comparable range. HNTs do not present any significant absorption in the visible region. Therefore, no apparent effect on the band energy is expected,[35] in accordance with other semiconductor/clay nanocomposites.[54] This observation differs from the red shifted E_g value observed in bentonite/g-C_3N_4 composites compared to the pure g-C_3N_4.[26] The corresponding plots used to calculate the band gap energies are given in Fig. S6B.

Zeta potential analysis was carried out to study the surface charge of the pure and nanocomposite materials. The negative charge of the nanocomposites is constantly higher than that of the pure g-C_3N_4 sample in the whole pH range > 3.5. As implied in Fig. S7, this most luckily originates from the more negative surface of the HNTs at the same pH range.

Photocatalytic activity

The photocatalytic efficiency of the pure and nanocomposite materials prepared was evaluated for the degradation of neutral, positively and negatively charged organic substrates under both simulated solar and pure visible light irradiation. For this purpose, phenol, MB and MO were used as model pollutants. Fig. S8 presents the kinetics of MB adsorption on the pure g-C_3N_4, HNTs and CNH-*x* nanocomposites over a period of 1.5 h in the dark. In all cases, adsorption/desorption equilibrium is reached approximately within 30 min of incubation. The addition of HNTs has a clear beneficial effect on adsorption. A linear increase of MB adsorption was observed with increasing HNTs content in the nanocomposite.

RSC Advances Accepted Manuscript

A four-fold increase was observed in the CNH-4 compared with the pure CN material. In this regard, the increase of the surface area in the nanocomposites (Table 1) can have an impact. However, the increased adsorption is most likely driven by the electrostatic attraction between the negatively charged external surface of HNTs and the positively charged MB. This is further supported by the adsorption experiments of MB on the pure HNTs. When the same amount of HNTs (0.125 g L^{-1}) present in the CNH-4 sample (e.g. ~10% HNTs) was used, MB adsorption approximately equals that of CNH-4 plus the pure g-C_3N_4 (black symbols in Fig. S8). However, when 1.25 g L^{-1} of pure HNTs were used (e.g. equal concentration with the nanocomposites) complete adsorption of MB is accomplished within less than 5 min (data not shown). These results clearly indicate that the enhanced adsorption of MB on the CNH-*x* series originate from the presence of HNTs in the nanocomposites.

The photocatalytic results under simulated sunlight irradiation are presented in Fig. 5A. Control experiments in the absence of light or catalyst verified that the observed decrease in the MB concentration is due a photocatalytic process. The catalytic data show a clear increase in MB degradation in the presence of the HNTs/g-C_3N_4 nanocomposites. This increase reaches a maximum for the CNH-2 catalyst (the one containing 4 wt.% of HNTs). Further increase of the HNTs content did not result in further enhancement which might be related with shading effects caused by excess HNTs loading and the decrease of the active phase content (e.g. g-C_3N_4). In addition, taking into account the surface area of the prepared nanocomposites, CNH-2 presented the highest photoactivity although CNH-4 has higher surface area (Table 1). This indicates that although the increased surface area might have an impact in photoactivity it is not the determinant factor controlling activity.

The rate constants (*k*) were obtained by assuming that the reaction follows a first order kinetics. The experimental data were fitted with the following equation

$$\ln\left(\frac{C_0}{C}\right)=kt$$

where *k* is the apparent first-order rate constant (min^{-1}), *t* is the irradiation time (min), C_0 is the initial concentration and *C* the concentration at reaction times *t*. The linearity observed in the kinetic plots expressed as $\ln(C_0/C)$ *vs.* irradiation time (*t*) (Fig. S9) verified that the degradation follows first-order kinetics. The kinetic constant is 3 times higher in the CNH-2 than the pure g-C_3N_4 sample.

It is well known that photocatalytic activity is greatly affected by adsorption capacity of the catalyst. Fig. 5B compares the adsorption capacity of the prepared materials with the rate constants as a function of the HNTs content in the nanocomposites. Worth of mentioning is that the color of the materials collected after the adsorption experiments was blue while after the catalytic runs the color was similar to the fresh catalyst implying that no MB remained adsorbed during irradiation. From the data in Figure 5B it can be concluded that enhanced adsorption on the CNH-*x* nanocomposites results in enhanced photoactivity when compared with the pure CN

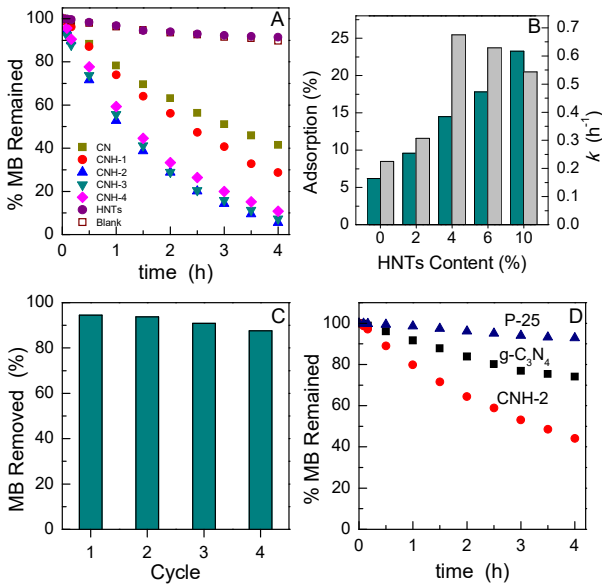

Fig. 5 A) Photocatalytic degradation of MB over the g-C_3N_4 and CNH-*x* photocatalysts under solar light irradiation after adsorption/desorption equilibrium was achieved. B) MB adsorption after 1.5 h incubation (blue bars) and the rate constants of MB degradation (gray bars). C) The catalytic stability test of the CNH-2 photocatalyst. MB degradation efficiency after 4 h simulated solar light irradiation for four consecutive reaction processes. D) Photocatalytic degradation of MB over the pure g-C_3N_4, CNH-2 nanocomposite and P-25 under pure visible light irradiation (λ> 420 nm).

material. However, although the CNH-2 catalyst showed the maximum catalytic activity, the adsorption capacity in the dark was 15 and 23 % for the CNH-2 and CNH-4 catalyst, respectively. This suggests that factors other than adsorption such as the actual g-C_3N_4 content and the shading effect caused by excess HNTs loading might have an impact in photoactivity. Alternatively, the higher adsorption with no concomitant enhanced catalytic activity may originate from the presence of isolated HNTs in the high loaded sample (i.e. CNH-4).

The stability of the HNTs/g-C_3N_4 nanocomposites was evaluated by recycling the CNH-2 material towards the photocatalytic decomposition of MB under simulated solar light irradiation for four times. As shown in Fig. 5C, the loss of the photocatalytic activity is negligible (approximately 7% after four consecutive runs) indicating the excellent photocatalytic stability of the prepared nanocomposites under the conditions of our experiment.

In addition to the catalytic tests under artificial solar light, selected materials were also tested under pure visible light irradiation (λ> 420 nm). Fig. 5D presents the time dependence of MB degradation for the pure g-C_3N_4 reference and the CNH-2 nanocomposite. As it is evidenced, the prepared catalysts were proven active under pure visible light irradiation. The CNH-2 catalyst showed superior photoactivity also under these conditions. As a reference, the photocatalytic activity under visible light irradiation of the commercial available TiO_2 Degussa P-25 catalyst is also presented. P-25 showed essentially no activity under these conditions, in accordance with its relatively wide band-gap energy (approximately 3.0

RSC Advances Accepted Manuscript

This journal is © The Royal Society of Chemistry 20xx

eV),[55] demonstrating also the absence of dye sensitization phenomena.

The prepared hybrids were also tested under solar light irradiation for the photodegradation of neutral and negatively charged organic substrates. Fig. S10A presents the photodegradation of phenol, a more stable and neutral (under the conditions of our experiment) pollutant. As it is evidenced, both g-C_3N_4 and the CNH-2 catalyst were proven active for the photodegradation of phenol. However, a clear enhancement is observed using the HNTs/g-C_3N_4 hybrid with respect to the reference material. In addition, the decomposition of the colorless phenol further demonstrates the absence of dye sensitization phenomena.

Catalytic reactions were also contacted over the pure g-C_3N_4 and the CNH-2 catalysts using a negatively charged substrate. In these experiments MO was used as the target model pollutant. Dye sensitization process scarcely occurs using MO since it is hardly excited under visible light irradiation compared with other dyes.[24] Before proceeding with the analysis of the catalytic data, of importance is to mention that in contrast to MB, MO presented zero adsorption on the pure HNTs either using high (1.25 g L^{-1}) or low (0.125 g L^{-1}) HNTs concentration. This explains the similar adsorption capacity of both g-C_3N_4 and CNH-2 for MO in the dark (~4-6 %). In Fig. S10B it is observed that both catalysts tested are active for the photodegradation of MO, further demonstrating the absence of dye sensitization processes in the pure g-C_3N_4 and the HNTs/g-C_3N_4 nanocomposites.[24] However, in this case the photoactivity of CNH-2 is only slightly higher than the pure reference g-C_3N_4. The clear beneficial effect of HNTs in the nanocomposites observed for the photodegradation of the positively charged MB (i.e. ×3 higher, Fig. 5B) and the neutral phenol is diminished in the case of the negatively charged MO. Considering that the reactions using different dyes were conducted under identical condition and that photocatalysis is expected to be driven by the same mechanism (see in the following), this difference can be attributed to the electrostatic attractive and repulsion forces between the HNTs' negatively charged surface and the MB and MO, respectively. In the case of MB, HNTs bring in contact the active phase of the catalyst (i.e. g-C_3N_4) with the substrate as demonstrated by the enhanced adsorption of MB in the nanocomposites and pure HNTs (Fig. S8), facilitating activity. In the case of phenol, such electrostatic interactions do not take place and therefore are not expected to have any impact in photoactivity.

Photocatalytic mechanism

To get insights into the reaction mechanism and to identify and assess the contribution of the active species, control experiments were conducted using scavengers for the photogenerated holes and free radicals over the most active CNH-2 catalyst and the pure g-C_3N_4 reference sample. Isopropanol (IPA) and *tert*-butyl alcohol (TBA) were used as h^+ and hydroxyl radical ($OH^{\cdot}$) scavengers, respectively.[56,57] To study the effect of superoxide radicals ($O_2^{-\cdot}$) on photoactivity, control experiments under saturated argon atmosphere were performed, maintaining anaerobic environment throughout the reaction. The effect of the various scavengers on the photocatalytic performance is presented in Fig. 6. In both cases, $OH^{\cdot}$ have no significant effect on the photocatalytic reaction. The photocatalytic degradation of MB is affected by the presence of both IPA and Ar, while the effect of Ar (*via* eliminating the formation of $O_2^{-\cdot}$) seems more prominent, suggesting that photogenerated electron-induced reduction of O_2 towards the production of $O_2^{-\cdot}$ dominates the photocatalytic degradation. These results clearly indicate that in both systems, photocatalytic activity is governed by the same mechanism.

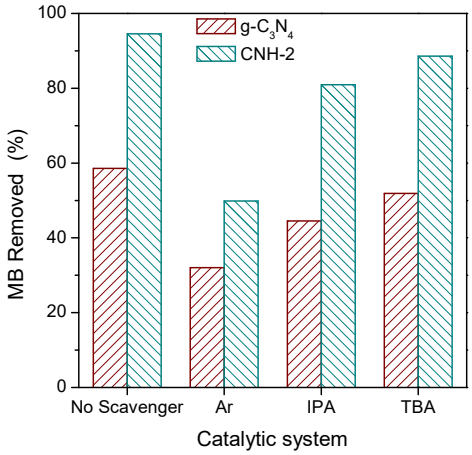

Fig. 6 Removal of MB by the reference g-C_3N_4 and the CNH-2 nanocomposite after 4h solar-light irradiation in the presence of various scavengers.

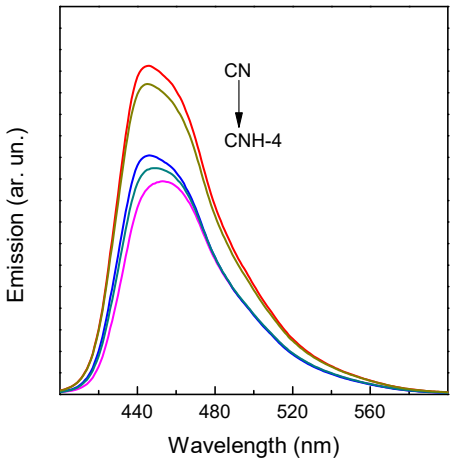

Fig. 7 Photoluminescence emission spectra of the pure g-C_3N_4 and the CNH-*x* nanocomposites.

Photocatalytic activity of semiconductors is defined by their ability to produce charge carriers which depends primarily on the semiconductor band gap and excitation

RSC Advances Accepted Manuscript

energy. Among the different principal photo-excitation processes, the ability to separate efficiently the photogenerated charges is considered essential for photocatalysis.[58] Herein, in an effort to investigate the charge generation and separation process, PL spectra of the prepared materials were recorded.

PL emission spectra of the pure g-C_3N_4 and the CNH-*x* nanocomposites are displayed in Fig. 7. One main emission peak centered approximately at 446 nm is attributed to the E_g of g-C_3N_4. As evidenced in Fig. 7, the presence of HNTs resulted into two distinct cases that show resemblance with the trend of the catalytic activity. The catalysts with significant increased catalytic activity as compared with the reference sample showed an important decrease in the PL emission intensity. The difference in the PL emission intensity is a direct evidence for the reduction of the photogenerated charges recombination rate with a direct effect in photoactivity.

Photocatalytic activity is a result of different factors including specific surface area, adsorption capacity with respect to the substrate, dispersion of the catalyst in the catalytic mixture, band gap energy, band edges energy level, charge carrier migration and separation and many others. Herein, the mild conditions applied to modify the parent material resulted to practically unchanged materials regarding the photoactive phase and small increase of the specific surface area. Nevertheless, specific differences between the pure and the HNTs modified g-C_3N_4 were detected, particularly in the abundance and stability of the photogenerated charge carriers. Halloysite cannot be excited under irradiation and considering that it is electrical insulator photogenerated charges formed on g-C_3N_4 cannot be transferred to HNTs. Therefore, the reduced recombination rates observed in the HNTs/g-C_3N_4 are related with the specific interaction between the two components in the heteroarchitectures. This can be ascribed to the electrostatic interaction between the negatively charged HNTs surface and the photogenerated e^- and h^+ in g-C_3N_4. In a scheme like this, electrostatic repulsion and attraction forces would result in the efficient migration and separation of e^- and h^+ on g-C_3N_4. A schematic diagram is presented in Fig. 8. The efficiently separated photogenerated e^- and h^+ result in enhanced photoactivity. This mechanism applies on charged and neutral organics. A similar mechanism has been suggested for bentonite/g-C_3N_4[31] and Ag_3PO_4/bentonite composites.[39] Besides acting as a charge carrier separator, HNTs serve also a second role. The negatively charged external surface of the HNTs results in high adsorption of cationic substrates. As a consequence, the coupling of HNTs with g-C_3N_4 brings MB in close vicinity to g-C_3N_4 where the active species are generated, facilitating photocatalysis.[42] This mechanism does not occur with neutral molecules. On the contrary, in negatively charged organics the negative impact on photoactivity due to the repulsion forces formed is neutralized with the enhanced activity due to charged separation, resulting to practically similar photoactivity of the reference g-C_3N_4 and the HNTs/g-C_3N_4 hybrids against MO. Overall, HNTs/g-C_3N_4 nanocomposites take advantage of the dual function of HNTs acting both as efficient photo-excited charge carrier separator and absorber for positively charged substances resulting in superior photoactivity.

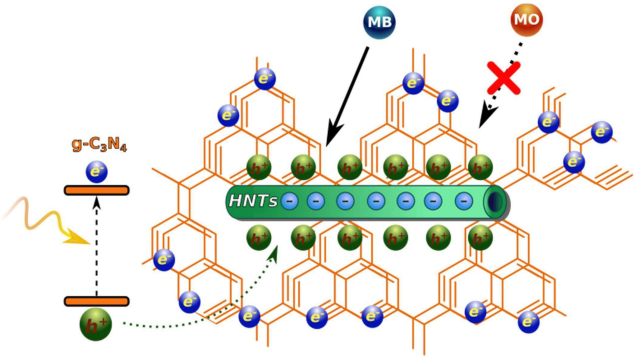

Fig. 8 Proposed mechanism for the enhanced charge carriers separation in the HNTs/g-C_3N_4 nanocomposites.

Conclusions

HNTs/g-C_3N_4 heteroarchitectures were developed by a facile and soft self-assembly strategy. The prepared nanocomposites were proven durable and exhibited higher photocatalytic activity for the degradation of neutral and positively charged organic molecules under both solar and pure visible light irradiation. PL spectra provided critical information for the recombination rate of photogenerated charges. The higher photoactivity of the nanocomposites is primarily attributed to the improved charge handling properties resulting in enhanced e^- and h^+ pairs formation due to electrostatic interaction with the negatively charged HNTs surface. In the case of positively charged organics, HNTs had a dual function: a) enhancing the abundance and stability of the photogenerated charges; b) promoting the adsorption of MB on the nanocomposite. Both functions are driven by electrostatic attractive and repulsion forces originating by the negatively charged HNTs surface.

Acknowledgements

K.C.C. acknowledges the TALENTS FVG Programme for a Post-doctoral fellowship funded from the European Social Fund (Operational Programme 2007-2013, Objective 2 Regional Competitiveness and Employment, Axis 5 Transnational cooperation, TALENTS FVG Programme). K.C.C., M.M., T.M. and P.F. acknowledge the financial support from the University of Trieste (through the FRA2015 project), ICCOM-CNR and INSTM Consortium.

Notes and references

1 D. Ollis, P. Pichat and N. Serpone, *Appl. Catal. B*, 2010, **99**, 377.
2 G. Marci, E.I. Garcia-Lopez and L. Palmisano, *Chem. Commun.*, 2014, **53**, 38.
3 V. Augugliaro, L. Palmisano, *ChemSusChem*, 2010, **3**, 1135.

This journal is © The Royal Society of Chemistry 20xx

RSC Advances Accepted Manuscript

4 M. Melchionna, A. Beltram, T. Montini, M. Monai, L. Nasi, P. Fornasiero and M. Prato, *Chem. Commun.*, 2016, **52**, 6977.
5 A. Di Paola, E. Garcia-Lopez, G. Marcì and L. Palmisano, *J. Hazard. Mater.*, 2012, **211-212**, 3.
6 A. Kubacka, M. Fernandez-Garcia and G. Colon, *Chem. Rev.*, 2012, **112**, 1555.
7 K.C. Christoforidis, S.J.A. Figueroa and M. Fernandez-Garcia, *Appl. Catal. B*, 2012, **117-118**, 310.
8 X.C. Wang, K. Maeda, A. Thomas, K. Takanabe, G. Xin, J.M. Carlsson, K. Domen and M. Antonietti, *Nat. Mater.*, 2009, **8**, 76.
9 W-J. Ong, L-L. Tan, S-P. Chai and S-T. Yong, *Chem. Commun.*, 2015, **51**, 858.
10 S.C. Yan, Z.S. Li and Z.G. Zou, *Langmuir*, 2009, **25**, 10397.
11 X. C. Wang, K. Maeda, A. Thomas, K. Takanabe, G. Xin, J. M. Carlsson, K. Domen and M. Antonietti, *Nat. Mater.*, 2009, **8**, 76.
12 Z. Zhao, Y. Sun and F. Dong. *Nanoscale*, 2015, **7**, 15.
13 J. Zhang, Y. Chen and X. Wang, *Energy Environ. Sci.*, 2015, **8**, 3092.
14 Y. Zheng, L. Lin, B. Wang and X. Wang, *Angew. Chem. Int. Ed.*, 2015, **54**, 12868.
15 Z. Ding, X. Chen, M. Antonietti and X. Wang, *ChemSusChem*, 2011, **4**, 274.
16 Y.J. Zhang, T. Mori, J.H. Ye and M. Antonietti, *J. Am. Chem. Soc.*, 2010, **132**, 6294.
17 S. Bai, X. Wang, C. Hu, M. Xie, J. Jiang and Y. Xiong, *Chem. Commun.*, 2014, **50**, 6094.
18 J.H. Sun, J.S. Zhang, M.Z. Zhang, M. Antonietti, X.Z. Fu and X.C. Wang, *Nat. Commun.*, 2012, 1139.
19 Y. Zhao, F. Zhao, X. Wang, C. Xu, Z. Zhang, G. Shi and L. Qu, *Angew. Chem. Int. Ed.*, 2014, **53**, 1.
20 D. Zheng, G. Zhang and X. Wang, *Appl. Catal. B*, 2015, **179**, 479.
21 D. Zheng, C. Pang, Y. Liu and X. Wang. *Chem. Commun.*, 2015, **51**, 9706.
22 K.C. Christoforidis, T. Montini, E. Bontempi, S. Zafeiratos, J.J. Delgado Jaen and P. Fornasiero, *Appl. Catal. B*, 2016, **187**, 171.
23 G. Zhang, Z-A. Lan, L. Lin, S. Lina and X. Wang, *Chem. Sci.*, 2016, **7**, 3062.
24 J. Fu, B.B. Chang, Y.L. Tian, F.N. Xi and X.P. Dong, *J. Mater. Chem. A*, 2013, **1**, 3083.
25 Y. He, L. Zhang, X. Wang, Y. Wu, H. Lin, L. Zhao, W. Weng, H. Wand and M. Fan, *RSC Adv.*, 2014, **4**, 13610.
26 Y. Li, J. Zhan, L. Huang, H. Xu, H. Li, R. Zhang and S. Wu, *RSC Adv.*, 2014, **4**, 11831.
27 M. Cargnello, M. Grzelczak, B. Rodriguez-Gonzalez, Z. Syrgiannis, K. Bakhmutsky, V. La Parola, L.M. Liz-Marzan, R.J. Gorte, M. Prato and P. Fornasiero, *J. Am. Chem. Soc.*, 2012, **134**, 11760.
28 J. Li, M. Zhou, Z. Ye, H. Wang, C. Ma, P. Huo and Y. Yan, *RSC Adv.*, 2015, **5**, 91177.
29 Z. Wang, F. Zhang, Y. Yang, B. Xue, J. Cui and N. Guan, *Chem. Mater.*, 2007, **19**, 3286.
30 J.T. Jin, X.G. Fu, Q. Liu and J.Y. Zhang, *J. Mater. Chem. A*, 2013, **1**, 10538.
31 K.C. Christoforidis, A. Kubacka, M. Ferrer, M.L. Cerrada, Marta Fernandez-Garcia and M. Fernandez-Garcia, *RSC Adv.*, **3**, 8541.
32 D. Papoulis, S. Komarneni, D. Panagiotaras, E. Stathatos, D.Toli, K.C. Christoforidis, M. Fernández-García, H. Li, Y. Shu, T. Sato and H. Katsuki, *Appl. Catal. B*, 2013, **132-133**, 416.
33 D. Papoulis, S. Komarneni, D. Panagiotaras, E. Stathatos, K.C. Christoforidis, M. Fernández-García, H. Li, Y. Shu, T. Sato and H. Katsuki, *Appl. Catal. B*, 2014, **147**, 526.
34 J. Ma, Q. Liu, L. Zhu, J. Zou, K. Wang, M. Yang and S. Komarneni, *Appl. Catal. B*, 2016, **182**, 26.
35 C. Li, J. Wang, S. Feng, Z. Yang and S. Ding, *J. Mater. Chem. A*, 2013, **1**, 8045.
36 R. Wang, G. Jiang, Y. Ding, Y. Wang, X. Sun, X. Wang and W. Chen, *ACS Appl. Mater. Interfaces*, 2011, **3**, 4154.
37 E. Joussein, S. Petit, J. Churchman, B. Theng, D. Righi and B. Delvaus, *Clay Miner.*, 2005, **40**, 383.
38 Y.M. Lvov, D.G. Shchukin, H. Mohwald and R.R. Price, *ACS Nano*, 2008, **2**, 814.
39 D.G. Shchukin, G.B. Sukhorukov, R.R. Price and Y.M. Lvov, *Small*, 2005, **1**, 510.
40 H. Lun, J. Ouyang and H. Yang, *RSC Adv.*, 2014, **4**, 44197.
41 G. Cavallaro, G. Lazzara, S. Milioto, F. Parisi and V. Sanzillo, *ACS Appl. Mater. Interfaces*, 2014, **6**, 606.
42 E. Abdullayev, R. Price, D. Shchukin and Y. Lvov, *ACS Appl. Mater. Interfaces*, 2009, **7**, 1437.
43 E. Abdullayev, K.Sakakibara, K. Okamoto, W. Wei, K. Ariga and Y. Lvov, *ACS Appl. Mater. Interfaces*, 2011, **3**, 4040.
44 L. Wang, J. Chen, L. Ge, Z. Zhu and V. Rudolph, *Energy Fuels*, 2011, **25** 3408.
45 K. Bourikas, J. Vakros, C. Kordulis and A. Lycourghiotis, *J. Phys. Chem. B*, 2003, **107**, 9441.
46 K.C. Christoforidis, A. Sengele, V. Keller and N. Keller, *ACS Appl. Mater. Interfaces*, 2015, **7**, 19324.
47 P. Yuan, P.D. Southon, Z. Liu, M.E.R. Green, J.M. Hook, S.J. Antill and C.J. Kepert, *J. Phys. Chem. C*, 2008, **112**, 15742.
48 M. Kim, S. Hwang and J.-S. Yu, *J. Mater. Chem.*, 2007, **17**, 1656.
49 G. Beamson, D. Briggs, High resolution XPS of organic polymers, The scienta ESCA A300 database, Wiley, Chichester (1992)
50 S. Zeng, C. Reyes, J. Liu, P.A. Rodgers, S.H. Wentworth and L. Sun, *Polymer*, 2014, **55**, 6519.
51 P. Sun, G. Liu, D. Lv, X. Dong, J. Wu, D. Wang, *RSC Adv.*, 2015, **5**, 52916.
52 J. Gonzalez-Ausejo, E. Sanchez-Safont, J. Gamez-Perez and L. Cabedo, *J. Appl. Polym. Sci.*, 2016, **133**, 42390.
53 W-J. Ong, L-L. Tan, S-P. Chai, S-T. Yong and A.R. Mohamed, *Nano Energy*, 2015, **13**, 757.
54 [41] C. Belver, J. Bedia, J.J. Rodriguez, *Appl. Catal. B*, 2015, **176**-**177**, 278.
55 K.C. Christoforidis, A. Iglesias-Juez, S.J.A. Figueroa, M. Di Michiel, M.A. Newton and M. Fernandez-Garcia, *Catal. Sci. Technol.*, 2013, **3**, 626.
56 L. Amirav and A.P. Alivisatos, *J. Phys. Chem. Lett.*, 2010, **1**, 1051.
57 S. Hu, R. Jin, G. Lu, D. Liu and J. Gui, *RSC Adv.*, 2014, **4**, 24863.
58 K.C. Christoforidis and M. Fernández-García, *Catal. Sci. Technol.*, 2016, **6**, 1094.

RSC Advances Accepted Manuscript

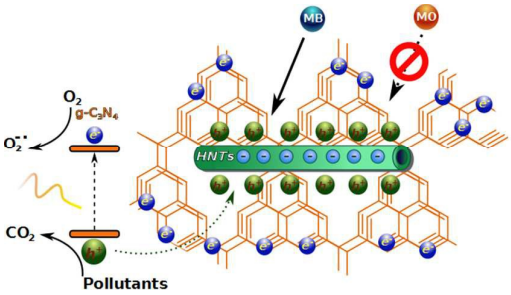

The charged surface of HNTs allows efficient charge separation and increased pollutants adsorption enhancing the overall HNTs/g-C_3N_4 heteroarchitectures photocatalytic performance.

RSC Advances Accepted Manuscript